# Increased Intraband Transitions in Smaller Gold Nanorods Enhance Light Emission

Behnaz Ostovar $^{\dagger}$ , Yi-Yu Cai $^{\sharp}$ , Lawrence J. Tauzin $^{\sharp}$ , Stephen A. Lee $^{\sharp}$ , Arash Ahmadivand $^{\dagger}$ , Runmin Zhang $^{\S}$ , Peter Nordlander $^{\dagger}$ , and Stephan Link $^{*\dagger}$ ;  $^{\sharp}$ 

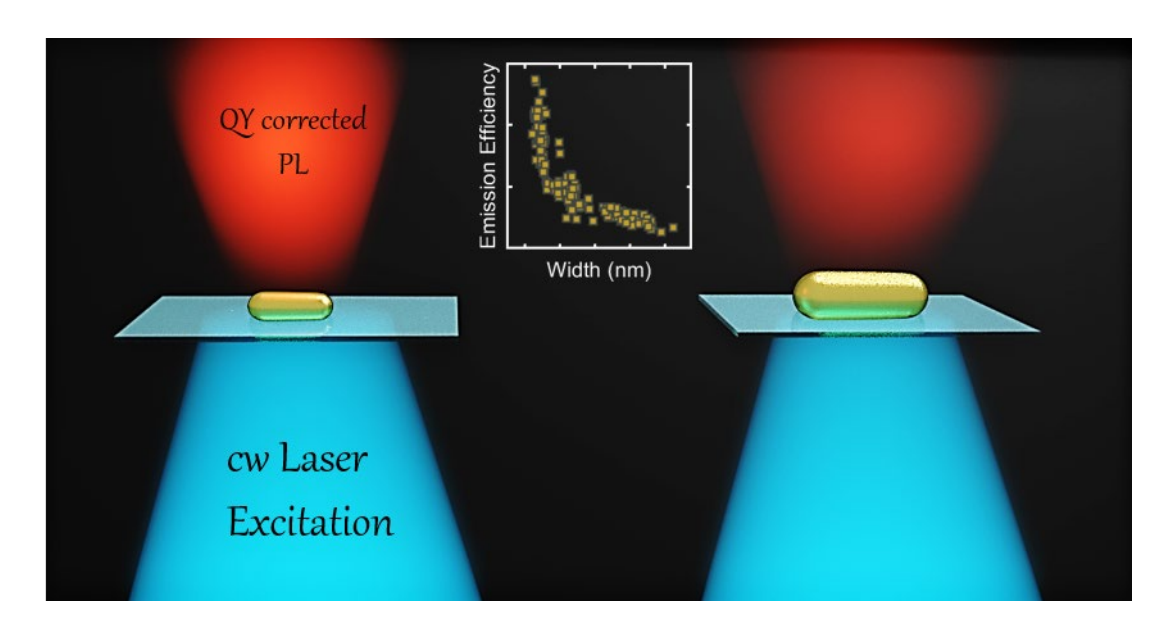
†Department of Electrical and Computer Engineering, ‡Department of Chemistry, §Department of Physics and Astronomy, †Department of Materials Science and NanoEngineering, ‡Laboratory for Nanophotonics, and \*Smalley-Curl Institute, Rice University, 6100 Main Street, Houston, Texas 77005, USA

\*Corresponding author email: slink@rice.edu

KEYWORDS: surface plasmon resonance, photoluminescence, interband transition, intraband transition, quantum yield, single-particle spectroscopy

ABSTRACT: Photoinduced light emission from plasmonic nanoparticles has attracted considerable interest within the scientific community because of its potential applications in sensing, imaging, and nanothermometry. One of the suggested mechanisms for the light emission from plasmonic nanoparticles is the plasmon enhanced radiative recombination of hot carriers through inter- and intraband transitions. Here, we investigate the nanoparticle size-dependence on the photoluminescence through a systematic analysis of gold nanorods with similar aspect ratios. Using single-particle emission and scattering spectroscopy along with correlated scanning electron microscopy and electromagnetic simulations, we calculate the emission quantum yields and Purcell enhancement factors for individual gold nanorods. Our results show strong size-dependent quantum yields in gold nanorods, with higher quantum yields for smaller gold nanorods. Furthermore, by determining the relative contributions to the photoluminescence from inter- and intraband transitions, we deduce that the observed size-dependence predominantly originates from the size-dependence of intraband transitions. Specifically, within the framework of Fermi's Golden rule for radiative recombination of excited charge carriers, we demonstrate that the Purcell factor enhancement alone cannot explain the emission size-dependence and that therefore changes in the transition matrix elements must also occur. Those changes are due to electric field confinement enhancing intraband transitions. These results provide vital insight into the intraband relaxation in metallic nanoconfined systems and therefore are of direct importance to the rapidly developing field of plasmonic photocatalysis.

# TOC:



Plasmonic nanoparticles have attracted significant attention in recent years because of their broad range of applications in sensing, 1-3 imaging, 4,5 nanothermometry, 6-8 photocatalysis, 9, 10 and photocurrent generation. 11, 12 The latter two applications rely on the generation of hot electrons and holes following photoexcitation. Distinct properties of hot electrons and holes have enabled different chemical processes: high energy hot electrons can induce bond dissociation reactions; 13, and hot holes can lead to oxidation. 15-17 Despite the recent progress, an improved understanding of how the distributions of hot electrons and holes evolve is still necessary and would enable the rational design of more efficient hot carrier based devices. 18-21

To date, several theoretical studies have demonstrated the dependence of hot carrier generation and distribution on the plasmonic nanoparticle geometry.<sup>20, 22-25</sup> Simulations have predicted efficient generation of hot holes in gold nanoslabs thicker than 40 nm through interband transitions, but size confinement can also increase the probability of hot electron generation *via* intraband transitions.<sup>20</sup> However, there are only a limited number of experimental results confirming enhanced intraband transitions in plasmonic nanostructures. For dimers of gold nanospheres it has been demonstrated that decreasing the gap size leads to stronger electric field confinement, allowing direct intraband transitions.<sup>26</sup> Similarly, in thin gold films and especially those with roughened surfaces giving rise to localized surface plasmon resonances (LSPRs) enhanced intraband transitions have been deduced from ultrafast pump-probe measurements and emission spectroscopy.<sup>27-28</sup> Based on these results, individual plasmonic nanoparticles with varying sizes are expected to be great candidates for a detailed investigation of size-dependent intraband transitions because the LSPR can be engineered in such a way that its spectral maximum remains almost constant while the associated electric field confinement varies strongly with size.

Due to the complexity of directly probing hot carriers, indirect methods for characterizing their properties have attracted attention.<sup>29, 30</sup> The light emission from plasmonic nanoparticles, due to the radiative recombination of hot electrons and holes generated through inter- and intraband transitions or photoluminescence (PL), presents a unique method for indirect characterization of hot carriers. <sup>29, 31, 32</sup> Using PL as a probe however requires an understanding of the mechanism and the relative contributions of inter- and intraband transitions. Emission from metal films was attributed to PL originating from interband transitions between the d-band and the sp-band near the L symmetry point of the Brillouin zone for bulk gold.<sup>33</sup> Momentum forbidden intraband transitions were reported to contribute to the PL as well, if the surfaces were rough and supported LSPRs.<sup>28, 34</sup> Emission from single AuNRs with well-defined plasmon modes has also been assigned to radiative recombinations of hot carriers via inter- or intraband transitions, 29, 35, 36 enhanced by plasmonic modes as quantitatively described with the Purcell effect mechanism.<sup>29, 30,</sup> <sup>32</sup> An alternative proposed mechanism argues that emission from metal nanoparticles is the result of electronic Raman scattering.<sup>37, 38</sup> A thorough study on the size-dependent contributions from inter- and intraband transitions to the emission is necessary to help further differentiate between these two mechanisms.

In this work, we investigate the PL of AuNRs with different widths but similar aspect ratios to determine the size-dependence of inter- and intraband transitions. Within the distribution of single AuNRs studied here, similar aspect ratios yield comparable longitudinal LSPR wavelengths and hence equivalent interband plasmon damping,<sup>39</sup> although retardation effects slightly redshift the longitudinal LSPR of the larger AuNRs.<sup>40, 41</sup> AuNRs of different sizes but similar aspect ratios

have been used to study size effects on surface enhanced Raman scattering<sup>42</sup> and chemical interface damping, 43 but only a limited number of AuNRs with similar aspect ratios have been studied and were found to show a slight increase in PL intensity with decreasing size.<sup>44</sup> However, the reason for the observed intensity increase has remained unclear.<sup>44</sup> We therefore prepared three different samples of colloidal AuNRs with aspect ratios of  $\sim$ 2 and with average dimensions of 29  $\pm$  2  $\times$  63  $\pm$  3, 45  $\pm$  5  $\times$  87  $\pm$  7, and 77  $\pm$  9  $\times$  153  $\pm$  9. We label single AuNRs by their width ranging from 25-35 as small, 40-55 nm as medium, and 65-100 nm as the large AuNRs. By combining dark field scattering (DFS), PL spectroscopy, and correlated scanning electron microscopy (SEM) we obtain a detailed understanding of the size-dependent PL in individual AuNRs. Experimental results are supplemented with simulations of PL spectra and absorption cross sections based on the correlated SEM images. From the absorption cross sections and PL photon counting we calculate emission quantum yields (QYs) of individual AuNRs to directly compare absolute PL intensities for different sizes. We find a size-dependent decrease of the PL QY with increasing AuNR size, in agreement with the emission mechanism based on Purcell effect enhanced radiative recombination of hot carriers. Only a weak size-dependence is seen for the interband component in the PL spectrum of AuNRs. Importantly, our results, supported by finite difference time domain (FDTD) simulations of electric fields inside the AuNRs, directly demonstrate that intraband transitions are enhanced in smaller AuNRs due to strongly confined electric fields.

### RESULTS AND DISCUSSION

Single-particle DFS and PL spectra were recorded for a number of particles from each sample and exhibited broadening of the DFS spectra and evolution of the PL lineshape as the size of the AuNRs increased. Representative DFS and PL spectra of small, medium, and large AuNRs are

presented in Figure 1A-C; the details for the characterization of length, width, and aspect ratio distributions of the three samples are presented in Figure S1. As the AuNR size increases, the DFS linewidth broadens due to increased radiation damping and, even though the aspect ratios are similar, there is a redshift of the longitudinal LSPR due to retardation effects (Figure 1A-C).<sup>31, 39, 45, 46</sup> The long wavelength resonance in the PL spectra follows the longitudinal LSPR seen in DFS, but is slightly blueshifted, in agreement with previous studies.<sup>29, 36, 44, 47, 48</sup> The blueshift of the PL emission spectra increases with increasing AuNR size (Figure 1A-C) and is quantified for all AuNRs in Figure S2. This resonance has contributions from both inter- and intraband transitions.<sup>29, 30, 35, 49</sup>

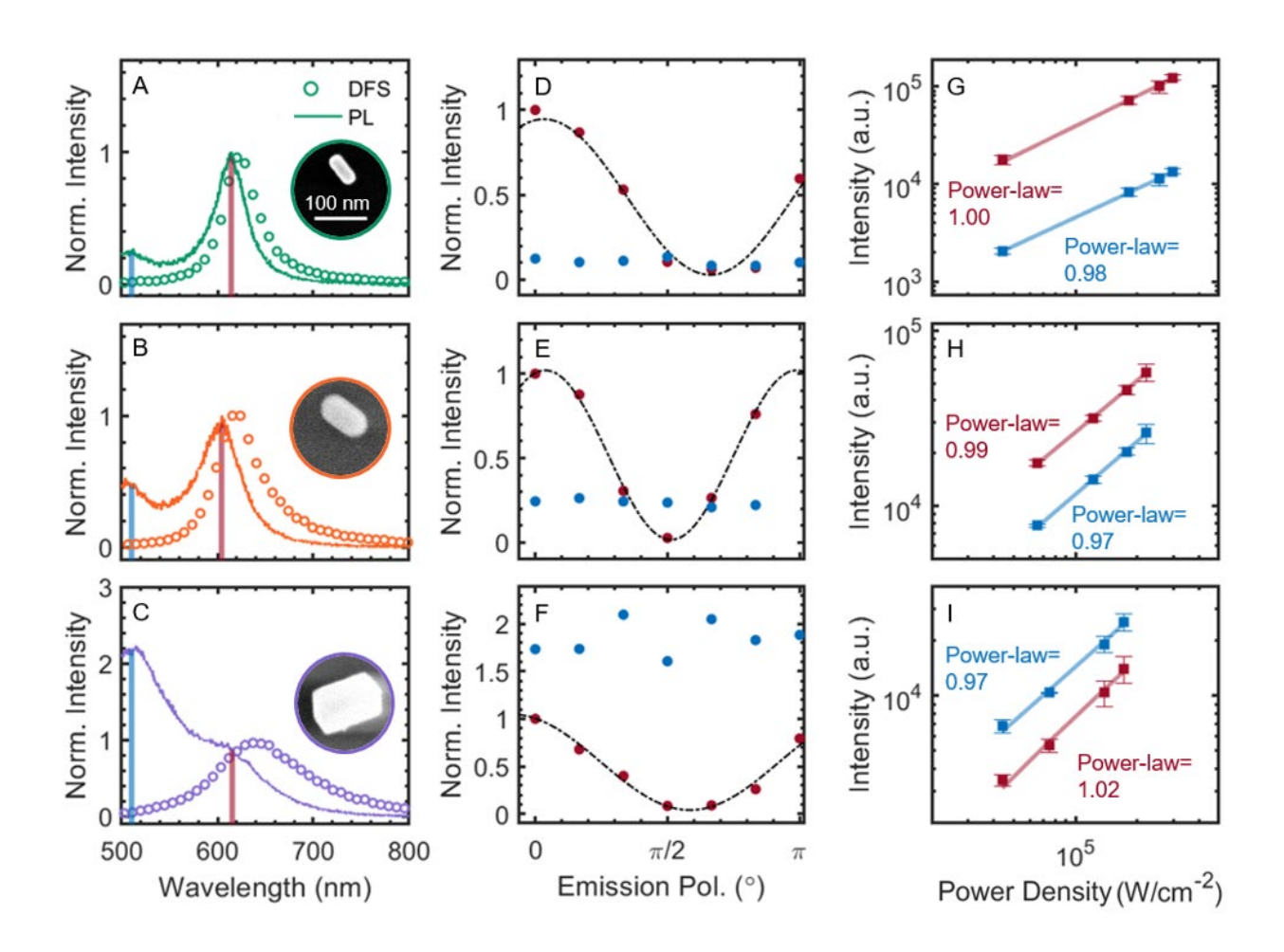


Figure 1. Representative correlated single-particle emission (line) and scattering (circles) spectra from small, medium, and large AuNR samples with sizes of (A)  $29 \times 63$  nm, (B)  $51 \times 104$  nm, and (C) 79 × 150 nm. Red and blue marked areas were used to investigate the polarization and power dependence of the emission at wavelengths corresponding to interband transitions and the LSPR spectral region, respectively. The corresponding SEM image of each AuNR is shown as insets. The spectra are intensity normalized at their corresponding long wavelength emission maximum to better illustrate spectral differences. (D-F) Emission polarization dependence for a representative small (D), medium (E), and large (F) AuNR for the interband transitions at  $510 \pm 3$ nm (blue circles) and close to the LSPR at the emission maximum  $\lambda_{max} \pm 3$  nm (red circles). The intensities are normalized to the corresponding value of the long wavelength emission maximum at 0° for each AuNR. The interband transitions are unpolarized, while emission at the LSPR follows that of a dipole emitter as demonstrated by the characteristic cos<sup>2</sup> intensity dependence as a function of polarizer angle (dotted black line). (G-I) Excitation power dependence of the emission for a representative small (G), medium (H), and large (I) AuNR. Excitation power dependence of the emission at 510  $\pm$  3 nm (blue squares) and  $\lambda_{max} \pm$  3 nm (red squares). A powerlaw dependence of one for the emission intensity as a function of excitation power for all AuNRs indicates a one-photon process for both spectral regions. The error bars shown were obtained by measuring the emission spectrum at every excitation power three times in random order.

The short wavelength feature in the PL spectra of the AuNRs, attributed to interband transitions, varies significantly relative to the long wavelength resonance. This emission is unpolarized (Figure 1D-F, blue dots) for all AuNR sizes, consistent with the assignment of interband transitions and a weak transverse plasmon mode with a reduced quality factor. In contrast, a strong dipolar emission

polarization dependence is observed for the long wavelength resonance, in agreement with previous reports.<sup>29, 31, 35, 44</sup> This behavior is consistent among the entire range of AuNR sizes as illustrated in Figures 1D-F and S3 for an exemplary AuNR from each of three samples. In Figures 1G-I and S4) we furthermore confirm that the emission for both short and long wavelength peaks is due to a one-photon process, as demonstrated by the linear PL intensity dependence on the excitation power.<sup>35, 50</sup>

The relative ratio between the emission intensities of these two peaks reverses as the AuNR size increases. The dominant resonance in the emission spectra of small AuNRs is found close to the longitudinal LSPR (Figure 1A), while for the large AuNRs, interband transitions dominate (Figure 1C). Note however that all spectra in Figure 1A-C are normalized at the long wavelength emission maximum to allow for a comparison between DFS and PL spectral features. As the PL intensity scales with the absorption cross section at the excitation wavelength of 488 nm, and hence with the volume of the AuNRs (Figure S5),<sup>51-53</sup> the intensities as measured cannot be quantitatively compared. However, by calculating the QYs of all individual AuNRs (see methods section) we are able to scale the PL spectra for a quantitative assessment of the size-dependence.

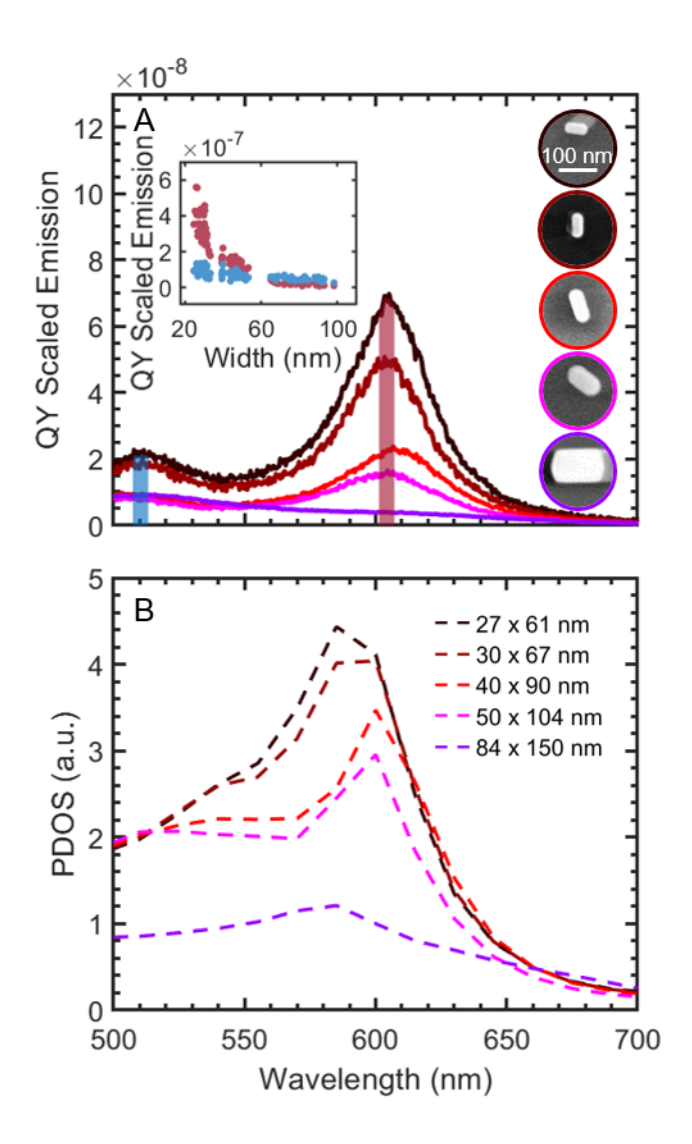


Figure 2. (A) Emission spectra of five AuNRs with different sizes scaled based on their QYs. SEM images of the corresponding AuNRs are given on the right. The sizes are  $27 \times 61$  nm,  $30 \times 67$  nm,  $40 \times 90$  nm,  $50 \times 104$  nm, and  $84 \times 150$  nm. Inset: Integrated intensity of the areas marked by the blue and red bars in the main figure for 120 AuNRs with different sizes; blue: centered at  $510 \pm 3$  nm and corresponding to the region where interband transitions dominate, red: at the emission resonance maximum  $\lambda_{max} \pm 3$  nm close to the longitudinal LSPR. (B) PDOS simulations carried out for AuNRs with the same sizes.

In contrast to what is suggested by the normalized spectra in Figure 1, once corrected by individual AuNR QYs a pronounced decrease in the intensity of the long wavelength emission peak is observed as the size increases, while the emission intensity for the interband transitions is relatively independent of size. Figure 2A shows emission spectra that are scaled by their respective QY for 5 different AuNRs chosen to cover the entire range of sizes. Clearly, the emission resonance close to the longitudinal LSPR drastically decreases in intensity with increasing AuNR size (red circles, inset of Figure 2A). Fermi's Golden rule states that emission is proportional to the photonic density of states (PDOS) and the transition matrix elements between the initial and final states.<sup>29, 47</sup> For larger particle sizes, the LSPR is broadened due to increased radiation damping, resulting in a decrease of the Purcell factor (which is proportional to the PDOS<sup>54</sup>), thus causing a decrease in the emission enhancement.<sup>31</sup> On the other hand, the interband emission does not follow a similar pronounced size-dependence compared to the emission at the longitudinal LSPR. The inset in Figure 2A shows the integrated emission corresponding to interband transitions for all AuNRs as a function of their width. Interband transitions are intrinsic properties of gold, and thus do not have a size-dependence when accounting for particle volume as done here. <sup>31, 55, 56</sup> The slight decrease in intensity observed with increasing size is likely the result of a weak interband emission enhancement by the transverse surface plasmon that is strongest for the smallest AuNRs, consistent with increased plasmon damping for larger AuNRs. 40, 57 For a more quantitative analysis of the emission enhancement as a function of AuNR size we will next focus on only the long wavelength resonance near the longitudinal LSPR.

The calculated PDOS of AuNRs with different sizes follows a similar trend as the experimental AuNR emission spectra (Figure 2B). The wavelength dependent PDOS were determined by

integrating the radiative PDOS calculated near the boundary of the AuNRs using the finite element method (COMSOL Multiphysics 5.4).  $^{29,58}$  As Figure 2B demonstrates, while the lineshape of the PDOS spectra deviates from that of the experimental emission spectra near the short wavelength feature, the main resonance peak close the longitudinal LSPR that we focus on here is successfully captured and the intensity decreases with increasing AuNR size. However, while the general trend is similar, the relative changes of PDOS intensities with increasing size are smaller than those of the experimental emission intensities near the longitudinal LSPR wavelength. Specifically, in the case of the AuNRs with dimensions of  $27 \times 61$  nm and  $50 \times 104$  nm in Figure 2B, the relative ratio of emission intensity yields a value of  $\sim 4.2$ , while the corresponding ratio for the calculated PDOS is only 1.5. Although an excess emission intensity decrease in ensemble measurements has been attributed to the re-absorption of emission, this phenomenon is negligible in single-particle emission measurements of AuNRs with similar sizes.  $^{44,59}$ 

The excellent agreement between PDOS and the experimental emission spectra achieved for smaller AuNRs is furthermore confirmed by simulations of PL spectra. PL spectra were simulated using our previously published model based on emission enhancement by the Purcell effect (see methods section).<sup>29</sup> A simulated PL spectrum is presented in Figure S6 and clearly shows that the spectral features of the experimental emission are well reproduced. Based on the simulated PL intensities of a total of eight AuNRs with varying sizes and the corresponding theoretical PDOS values at the longitudinal LSPR maximum, a linear dependence is established between PL intensity and PDOS for the small AuNRs, as illustrated in Figure S7. This linear dependence further strengthens our argument that for the entire AuNR size range the experimental PL intensities (Figure 2A) decrease more than expected based on PDOS alone (Figure 2B). We will furthermore

utilize this linear relationship between simulated PL intensity and PDOS for a more quantitative analysis below.

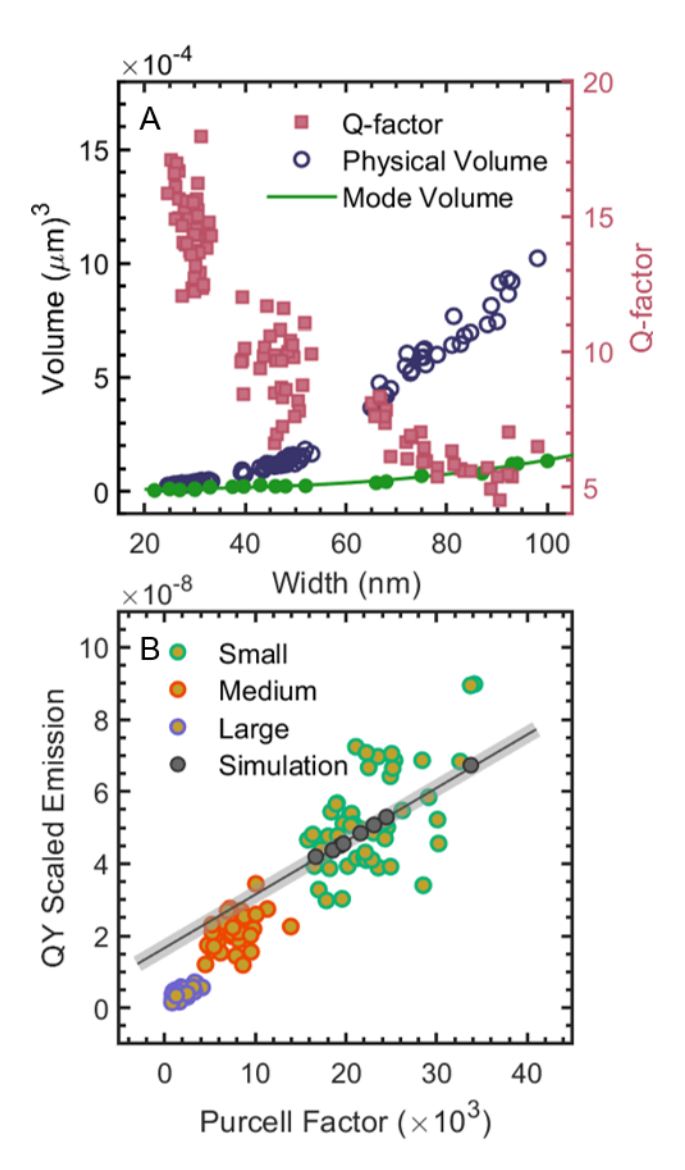


**Figure 3.** (A) Mode volume (green line and circles) and physical volume (blue circles) as a function of AuNR width. Mode volumes were calculated for 23 AuNRs with sizes chosen randomly from within the experimental distribution. Pink squares show the Q- factor of the same individual AuNRs obtained from their respective DFS spectra. (B) QY scaled emission of AuNRs at their long wavelength emission maxima wavelengths  $\pm$  0.5 nm as a function of Purcell factor.

Data points are color coded for the small (green), medium (orange), and large (purple) AuNR samples. Gray circles indicate the simulated PL intensities as a function of Purcell Factor after appropriately scaling the PDOS calculated at the long wavelength emission maximum, with the gray line showing a linear regression to the simulated data and extrapolation to all AuNR sizes. The shadowed area indicates the standard deviation. The symbol sizes were chosen to be on the order of the error for all data presented, including the Q–factor uncertainties estimated through error propagation of  $E_{\rm res}$  and  $\Gamma$ , uncertainties in AuNR widths and volumes as estimated based on the resolution of the SEM, and uncertainties in Purcell factor estimated through error propagation of the Q–factor and  $\lambda$  (Equation 1).

Further quantifying the different contributions of inter- and intraband transitions to the emission spectra of AuNRs confirms that the size-dependent PL arises from changes in the contribution from intraband transitions (Figure 3). Based on the Purcell effect PL mechanism, the emission enhancement is proportional to the simulated PDOS. Instead of simulating the PDOS as shown in Figure 2, the Purcell factor can also be derived experimentally using the following definition: <sup>54,</sup>

Purcell factor = 
$$\frac{3 Q - factor}{4\pi^2 V} \left(\frac{\lambda}{n}\right)^3$$
 (1)

Here the Q-factor is the quality factor of the cavity resonance (i.e., the AuNR), V describes the mode volume,  $\lambda$  is the emission wavelength, and n is the refractive index of the surrounding medium and was set to 1. The Q-factor is determined from the DFS spectra according to:  $^{39,61}$ 

$$Q-factor = \frac{E_{res}}{\Gamma}$$
 (2)

Here  $E_{res}$  is the resonance energy and  $\Gamma$  is the homogeneous linewidth of the longitudinal LSPR both obtained through fitting to a Lorentzian function. <sup>39, 61</sup> Figure S8 shows the details of the fitting to a Lorentzian function for three exemplary AuNRs with small, medium, and large sizes. The mode volumes were calculated following the approach proposed by Koenderink: <sup>54, 62</sup>

$$V = \frac{\int (Re\varepsilon + 2\omega Im\varepsilon/\gamma)|E|^2 dr}{max((Re\varepsilon + 2\omega Im\varepsilon/\gamma)|E|^2)}$$
(3)

In this procedure, the energy density is defined as  $(Re\varepsilon + 2\omega Im\varepsilon/\gamma) |E|^2$  for plasmonic nanostructures instead of  $\varepsilon |E|^2$  as is the textbook definition of the mode volume.<sup>54, 63</sup> The integral is calculated over all space, where |E| is the magnitude of the electric field,  $\omega$  is the frequency,  $\varepsilon$  is the complex dielectric function taken from Johnson and Christy, and  $\gamma$  is the Drude damping, for which we used a value of 0.07 eV.<sup>64, 65</sup>

The measured *Q-factors* and calculated mode volumes of the AuNRs are presented in Figure 3A. Smaller AuNRs have mode volumes (green line and circles) comparable to their physical volume (blue circles). However, as the size increases the mode volume significantly differs from the physical volume, increasing much more slowly than the actual size because the electric field is mainly confined near the metal surface. From these values we calculated the Purcell factors for different AuNR sizes using Equation 1. Figure 3B illustrates the resulting QY scaled emission intensities at the long wavelength resonance as a function of the Purcell factor for all 120 AuNRs investigated.

By increasing the AuNR size, the contribution from intraband transitions to light emission decreases. Based on the eight simulated PL spectra for small AuNRs discussed above, the gray circles in Figure 3B indicate the simulated PL intensity at the long wavelength resonance *versus* 

the calculated and scaled PDOS, recognizing the proportional relationship between PDOS and Purcell factor.<sup>54</sup> A linear interpolation of the simulated PL intensities and extrapolation to larger AuNR sizes predicts PL intensities based only on the enhancement by the PDOS and ignores any potential changes to the transition matrix elements, as indicated by the gray line in Figure 3B. This predicted trend is clearly not followed by the medium (Figure 3B, orange symbols) and large AuNRs (Figure 3B, purple symbols). Those deviations increase with increasing AuNR size, leading us to conclude that contributions from intraband transitions to their emission decrease. These results indicate that based on Fermi's Golden rule, the transition matrix elements change as a function of size, which we attribute to decreased intraband transitions in larger sizes due to momentum conservation rules, similar to the case of smooth gold films where intraband transitions are not allowed.<sup>28</sup> We next demonstrate that the observed size-dependent increase in the intraband contribution to the PL can be related to the stronger confinement of the electric field in the smaller AuNRs providing the necessary momentum for intraband transitions.

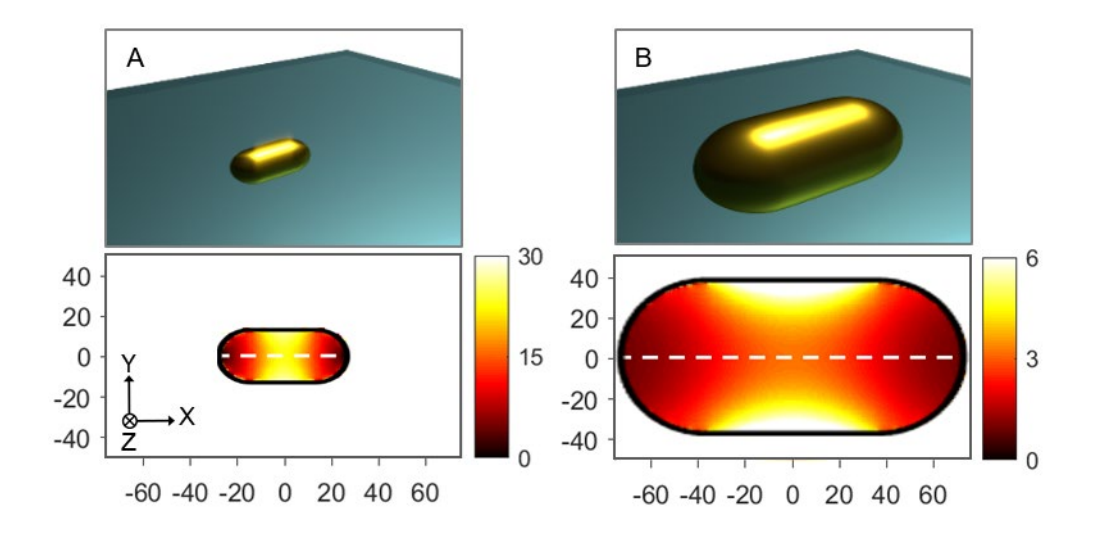


**Figure 4.** FDTD simulations of the  $|E|^2/|E_0|^2$  distribution in the near field inside the AuNRs calculated at the long wavelength resonance. Schematic illustration and  $|E|^2/|E_0|^2$  distributions for

inside of the simulated AuNRs with sizes of (A)  $27 \times 55$  nm and (B)  $75 \times 148$  nm representing the small and large AuNR samples, respectively. The black lines indicate the outside boundary of the AuNRs. White dashed lines indicate the line sections taken along the long AuNR axis (y-axis). The confinement of  $|E|^2/|E_0|^2$  is estimated as the distance d over which the electric field varies, where d is taken as the full width of the line section at half maximum.

The electric field confinement and its spatial nonuniformity in plasmonic nanoparticles can assist in enhancing intraband transitions by providing the necessary momentum. FDTD simulations for a small and a large AuNR were performed to obtain the electric field intensity distribution inside the AuNRs and to estimate the electric field confinement (Figure 4). The electric field distributions calculated for cross sections inside the AuNRs along their main axes at the corresponding long wavelength resonance wavelengths are more confined for the smaller AuNR (Figure 4A) compared to those of the larger AuNR (Figure 4B), in agreement with previous work. $^{66,67}$  The kvector of the confined electric field can be decomposed into components perpendicular and parallel to the metal surface,  $k_{\perp}$  and  $k_{\parallel}$  which can be written as  $k=\sqrt{k_{\parallel}^2+k_{\perp}^2}$ . In confined nanostructures  $|k_{\perp}|, |k_{\parallel}| \gg k.^{28}$  The wave vector with the largest magnitude present in the near field has been described using  $k_{\parallel} \approx \pi \, / d$ , where d corresponds to the distance over which the electric field varies.  $^{28,68}$  Based on our calculations, approximate values for d are 26 nm for the smaller AuNR (Figure 4A) and 66 nm for the larger AuNR (Figure 4B). The effective generation of intraband transitions reported for rough thin metal films with  $d \approx 5-30$  nm is comparable to the value obtained here for the small AuNR. 28 The derived  $k_{\parallel}$  for the smaller AuNR is approximately 12.0  $\times$  10<sup>7</sup> cm<sup>-1</sup> and 4.8  $\times$  10<sup>7</sup> cm<sup>-1</sup> for the larger AuNR. Using the parabolic approximation for the conduction band dispersion and an approximate value of 10<sup>8</sup> cm<sup>-1</sup> for the Fermi wave number in gold,<sup>28</sup> the momentum needed for exciting an electron in the sp-band to energy levels corresponding to the longitudinal LSPR of AuNRs with aspect ratio of 2 (*i.e.*, 1.96 eV above the Fermi level) is  $\Delta k \approx 7 \times 10^7$  cm<sup>-1</sup>. When  $\Delta k$  needed for intraband transitions and  $k_{\parallel}$  provided by the electric field distribution are of the same magnitude, direct excitation of electrons within the conduction band is possible.<sup>28</sup> Comparing  $\Delta k$  and  $k_{\parallel}$  of the two AuNRs supports that the emission spectra of the small AuNRs have a larger contribution from intraband transitions compared to the large AuNRs. Specifically, the calculated 2.3 times stronger electric field confinement in smaller AuNRs provides the necessary momentum mismatch to allow efficient radiative recombinations through intraband transitions compared to larger AuNRs with weaker electric field confinement. It has also been reported that other factors such as phonon coupling, the Umklapp process, and Landau damping can give rise to larger values of  $k_{\parallel}$  in small nanoparticles.<sup>27</sup> The analysis provided here further supports the conclusion that the increased PL intensity in smaller nanoparticles arises from an increase of intraband emission transitions that become allowed due to the nonuniformity of the internal electric fields.

# **CONCLUSIONS**

In summary, we conducted a systematic study of the size-dependence of light emission from AuNRs. Our approach utilizes AuNRs of different widths but similar aspect ratios and hence similar resonance energies for the longitudinal mode in order to have comparable contributions from interband damping.<sup>31</sup> Our single-particle DFS and PL spectroscopy along with the correlated SEM images reveal the importance of AuNR geometry on the emission spectra and QYs as well as on the relative contributions of inter- and intraband transitions to the PL. Our results suggest that, in small AuNRs, intraband transitions are allowed due to the increased electric field

confinement. While interband transitions are the dominant contribution in the emission of large AuNRs and are only weakly dependent on size, a noticeable decrease in the long wavelength emission of the large AuNRs is attributed to the decrease in the contribution from intraband transitions. Within the framework of Fermi's Golden rule for radiative recombination of excited charge carriers, our combined experimental and theoretical results clearly demonstrate that the Purcell factor enhancement alone cannot explain the PL size-dependence and that therefore changes in the transition matrix elements must also occur. Those changes are due to the increased intraband contribution assisted by the electric field confinement. Furthermore, we conclude that the observed size-dependence of the emission from AuNRs is consistent with an emission mechanism based on photoluminescence from hot carriers. The direct experimental demonstration of enhanced intraband transitions in confined metallic nanostructures provides important insight that can be used for characterizing and optimizing plasmon-induced hot carrier generation in photocatalysis and photocurrent applications.

# **METHODS**

**AuNR Sample Preparation.** Chemically synthesized AuNRs were selected from three samples with different sizes, but similar aspect ratios of ~2. The average sizes of the AuNRs in the three samples were  $29 \pm 2 \times 63 \pm 3$  nm,  $45 \pm 5 \times 87 \pm 7$  nm, and  $77 \pm 9 \times 153 \pm 9$ ; referred to as small, medium, and large respectively. Small and medium AuNRs were synthesized using a modified seed-mediated growth process developed by the Murray group.<sup>69</sup> The large AuNRs were synthesized based on a synthesis method by Ming *et al.*<sup>70</sup> Details of the two synthesis protocols are described in a previous publication.<sup>29</sup>

Indexed quartz slides were used as substrates because quartz has a reduced background in emission measurements and thus results in increased signal to noise ratios. A dilute base piranha solution (1:4:20 NH<sub>4</sub>OH/H<sub>2</sub>O<sub>2</sub>/H<sub>2</sub>O) was used to clean the quartz slides (AdValue Tech). The slides were rinsed twice with Millipore (DI) water and N<sub>2</sub> gas was used to dry the quartz substrates prior to gold evaporation for indexing. An indexed grid was patterned onto the quartz slides by evaporating 35 nm of gold through a TEM grid shadow mask (Ted Pella), enabling correlated single-particle measurements. The indexed quartz slides were then O<sub>2</sub> plasma-cleaned for 2 minutes. An appropriate concentration of AuNRs was spin-coated on the indexed quartz slides for 60 s at 2500 rpm for adequate single-particle coverage. In order to determine dimensions of the AuNRs, correlated SEM images of all individual AuNRs were obtained. SEM imaging was performed after all optical measurements using a FEI Quanta 400 ESEM FEG operated at a voltage of 30 kV in low-vacuum mode with a resolution of about 1.5 nm.

Dark Field Scattering and Photoluminescence Measurements. A home-built single-particle setup based on an inverted microscope (Zeiss Axio Observer.D1m) was used for all the single-particle measurements of this work.<sup>31</sup> In our correlated configuration, DFS measurements were conducted first. A wide field image recorded on a digital single-lens reflex camera was collected and the same image was later used to locate the particles in the DFS and PL spectroscopy measurements. A halogen lamp (Zeiss HAL 100) provided the excitation light that was focused on the sample with an oil immersion dark field condenser. A 50x air objective with a 0.8 numerical aperture (Zeiss EC Epiplan-Neofluar) was used to collect the scattered light. The light was passed through a pinhole with a 50 μm diameter (Thorlabs P50S) to achieve a confocal geometry by spatially filtering the light. A DFS image was constructed by moving the sample with a piezo scanning stage (Physik Instrumente P-517.3CL) and detecting the spatially filtered light on an

avalanche photodiode (APD, PerkinElmer SPCM-AQRH-15). Single-particle DFS spectra of the imaged particles were obtained by redirecting the signal of each particle to a spectrometer (Shamrock SR193i-A) connected to a charge-coupled device (CCD) camera (Andor iDus 420 BEX2-DD). The spectra, recorded with an integration time of 3 seconds, were background subtracted with signal from an area near the nanoparticle where no other nanoparticles were located. The spectra were furthermore corrected by the white light spectrum from the halogen lamp obtained by switching to the transmitted light mode of the condenser and recording the spectrum with the same CCD camera.

Correlated confocal emission images and spectra were collected immediately after measuring the corresponding DFS spectra using the same instrument. For emission spectroscopy, a 488 nm continuous wave diode laser (Coherent OBIS) was used as the excitation source and was directed to the sample with a 50/50 dichroic mirror (Chroma). The pinhole was removed from the detection path and a 488 nm notch filter (Semrock) together with a 496 nm long pass filter (Semrock) were employed to reject the excitation source and transmit the emission. A depolarizer (Edmund Optics Quartz Lyot Depolarizer) was placed before the spectrometer to remove any polarization bias. For each nanoparticle three emission spectra with a 20 second exposure time were collected and averaged. The background signal for each nanoparticle was then measured on a blank area near the nanoparticle. The emission spectra were analyzed after background subtraction and adjustment for detection efficiency. The detection efficiency of the setup for different wavelengths was corrected by using a calibrated lamp (Ocean Optics LS-1 Cal) as described previously. 71 The laser powers were measured after the objective at the sample plane. The laser beam size had a full width at half-maximum of ~400 nm as obtained from AuNR images. The excitation power density was limited to 1.1 × 10<sup>5</sup> W/cm<sup>-2</sup> to prevent damaging the nanoparticles. Larger excitation power densities were used in the power dependence measurements, but we always checked for nanoparticle damage by recording a second DFS spectrum after the emission measurements and only considering nanoparticles that showed no changes.

**Photoluminescence Simulations.** PL spectra were calculated according to a previously published model based on the Purcell effect:<sup>29</sup>

$$I(\omega) = \sum_{\varepsilon_i - \varepsilon_j = \omega} \Gamma_{i \to j}(\omega) P_i(1 - P_j) \rho_{\mathcal{E}}(\varepsilon_i) \rho_{\mathcal{E}}(\varepsilon_j) \rho_{\mathcal{P}}(\omega)$$
(4)

Where  $\Gamma_{i\to j}(\omega)$  denotes the transition rate between states i and j given by Fermi's golden rule. The energy dependence of the transition matrix elements was determined by parametrization with only one adjustable parameter and its value was fixed to 2.65 for all PL simulations.  $P_i$  indicates the probability of electron occupation of state i. The hot carrier excitation was determined by the electronic density of states  $\rho_E(\varepsilon_i)$  as well as the transition matrix elements.  $\rho_P(\omega)$  incorporates the enhancement effect of the calculated PDOS. A more detailed description of the PL simulation model has been published in ref [29]. Note that the simulated values of the PDOS (Figure S7) are proportional to the experimental Purcell factor as determined from Equation 1 and were appropriately scaled to be shown in Figure 3B.<sup>54</sup>

**Quantum Yield Calculation.** The emission QYs of the individual AuNRs were calculated according to a previously published method.<sup>71</sup> Here, the QY ( $\Phi$ ) is defined as the ratio of emitted photons ( $N_{em}$ ) to absorbed photons ( $N_{abs}$ ):

$$\Phi = \frac{N_{em}}{N_{abs}} \tag{5}$$

First, the raw photon counts ( $N_{raw}$ ) were determined by measuring photon counts obtained from APD images of single AuNRs in a 2  $\mu$ m by 2  $\mu$ m scanned area.  $N_{em}$  is then calculated by correcting  $N_{raw}$  for the wavelength dependent efficiencies of the optics and filters used ( $\Pi$ ) and photon detection efficiency of our detector (Det.Eff):

$$N_{em} = \frac{N_{raw}}{\Pi \cdot Det.Eff}$$
 (6)

A standard dye, rhodamine 6G, excited at 488 nm with a known absorption cross section and QY, was used to obtain a 1.6% Det.Eff for our setup. N<sub>abs</sub> is determined using:

$$N_{abs} = \frac{\sigma_{abs} I_{exc}}{h \nu_{exc}} \tag{7}$$

The excitation intensity ( $I_{exc}$ ) was found by measuring the power of the incident laser at the sample plane after the objective and dividing it by the beam waist. FDTD simulations were used to calculate the absorption cross section ( $\sigma_{abs}$ ) of each individual AuNR at the excitation wavelength based on the AuNR dimensions from SEM (Figure S5). Details regarding the FDTD simulations are discussed in the next section. The energy absorbed was converted into photons absorbed by dividing by the energy of the incident photons,  $ho_{exc}$ . The calculated QYs of individual AuNRs were then employed to scale the experimental emission spectra making it possible to directly compare all AuNRs acquired during different measurements. In the scaling procedure, integration of the emission spectra over the entire detected spectral region was first carried out. Spectral scaling was then performed in such a way that the integrated scaled PL spectrum is equal to the QY according to:

$$\Phi = \int \text{scaled PL spectrum} \tag{8}$$

Finite Difference Time Domain Simulations. The commercial software package Lumerical FDTD Solutions was employed to simulate absorption and scattering cross sections and electromagnetic field distributions of AuNRs. Each AuNR's geometry was approximated as a hemisphere capped cylinder, covered with a 3.5 nm cetyltrimethylammonium bromide shell accounting for the ligand molecules; the refractive index of this dielectric layer was set to 1.44.<sup>72</sup> The bulk gold dielectric function measured by Johnson and Christy was employed to describe the AuNRs,<sup>64</sup> sitting on a semi-infinite quartz substrate with a refractive index of 1.52.<sup>72</sup> The AuNRs

were illuminated using a total field scattered field source with a wave vector normal to the AuNR longitudinal axis. A 0.5 nm computational mesh size was chosen and the convergence criteria were set to default with perfectly matched layers to avoid errors arising from reflections at the boundaries. The absorption and scattering cross sections were determined by setting power monitors that allowed for calculation of the net power flow into the total and scattered field simulation domains. The electric field distributions at the longitudinal LSPR were assessed using the frequency domain field profile monitors.

For the absorption cross section simulations needed for the QY calculations, the dimensions of each AuNR were set equal to the sizes measured by the correlated SEM images and varied within  $\pm$  2 nm for small and medium AuNRs and  $\pm$  5 nm for large AuNRs to achieve the best match between the simulated scattering cross section maximum and the experimentally measured DFS maximum. The tolerable range for a match between simulation and experiment was when the maxima deviated by only  $\pm$  5 nm. As an example, Figure S9 shows simulated scattering cross sections and their acceptable agreement with the experimental DFS spectra for three representative AuNRs, one each from the small, medium, and large samples. After achieving such agreement, the absorption cross section of the AuNRs was determined at 488 nm and used in the QY calculations. Finite Element Method Simulations. The commercial package COMSOL Multiphysics 5.4 RF Module was employed to determine the radiative PDOS spectra projected to the far-field for AuNRs. The sizes obtained from the correlated SEM images were used to set the dimension of each AuNR. To define the boundary conditions, the entire workplace was encompassed by perfectly matched layers. In order to compute the PDOS spectra, a dipole source was utilized and the medium was assumed to be homogenous. When the dipole source is in resonance with the AuNR, the emission from the system can be calculated for different dipole orientations.

ASSOCIATED CONTENT

Supporting Information. The Supporting Information is available free of charge on the ACS

Publications website. Characterizations of the AuNR samples; further analysis of AuNR emission;

polarization and excitation power dependence of the emission spectra; FDTD simulated absorption

cross-sections; simulated PL spectra; Lorentzian fits of DFS spectra; FDTD simulated scattering

cross-sections. (PDF)

**AUTHOR INFORMATION** 

ORCID

Peter Nordlander: 0000-0002-1633-2937

Stephan Link: 0000-0002-4781-930X

**Present Address** 

Department of Electrical and Systems Engineering, University of Pennsylvania, Philadelphia,

Pennsylvania 19104, USA.

**Author Contributions** 

The manuscript was written through contributions of all authors. All authors have given approval

to the final version of the manuscript.

Notes

The authors declare no competing financial interest.

**ACKNOWLEDGMENTS** 

25

We acknowledge financial support from the Robert A. Welch Foundation (C-1222 to P.N. and C-1664 to S.L.), the Air Force Office of Scientific Research *via* the Department of Defense Multidisciplinary University Research Initiative, under Award FA9550-15-1-0022 to P. N and S.L., and the National Science Foundation (ECCS-1608917) to S.L. This work was conducted in part using resources of the Shared Equipment Authority at Rice University. We thank Nathan Diemle, Patrick Straney, and Jill Millstone for providing us with gold nanorod samples.

### REFERENCES

- 1. Tinguely, J.-C.; Sow, I.; Leiner, C.; Grand, J.; Hohenau, A.; Felidj, N.; Aubard, J.; Krenn,
- J. R., Gold Nanoparticles for Plasmonic Biosensing: The Role of Metal Crystallinity and Nanoscale Roughness. *J. Bionanosci.* **2011,** *I*, 128-135.
- 2. Kim, Y.; Johnson, R. C.; Hupp, J. T., Gold Nanoparticle-Based Sensing of "Spectroscopically Silent" Heavy Metal Ions. *Nano Lett.* **2001**, *1*, 165-167.
- 3. Lu, G.; Hou, L.; Zhang, T.; Liu, J.; Shen, H.; Luo, C.; Gong, Q., Plasmonic Sensing Via Photoluminescence of Individual Gold Nanorod. *J. Phys. Chem. C* **2012**, *116*, 25509-25516.
- 4. Carattino, A.; Keizer, V. I. P.; Schaaf, M. J. M.; Orrit, M., Background Suppression in Imaging Gold Nanorods through Detection of Anti-Stokes Emission. *Biophys. J.* **2016**, *111*, 2492-2499.
- 5. Wang, H.; Huff, T. B.; Zweifel, D. A.; He, W.; Low, P. S.; Wei, A.; Cheng, J.-X., In Vitro and in Vivo Two-Photon Luminescence Imaging of Single Gold Nanorods. *Proc. Natl. Acad. Sci. U. S. A.* **2005**, *102*, 15752-15756.
- 6. Xie, X.; Cahill, D. G., Thermometry of Plasmonic Nanostructures by Anti-Stokes Electronic Raman Scattering. *Appl. Phys. Lett.* **2016**, *109*, 183104.
- 7. Jones, S.; Andrén, D.; Karpinski, P.; Käll, M., Photothermal Heating of Plasmonic Nanoantennas: Influence on Trapped Particle Dynamics and Colloid Distribution. *ACS Photonics* **2018**, *5*, 2878-2887.
- 8. Carattino, A.; Caldarola, M.; Orrit, M., Gold Nanoparticles as Absolute Nanothermometers. *Nano Lett.* **2018**, *18*, 874-880.
- 9. Brongersma, M. L.; Halas, N. J.; Nordlander, P., Plasmon-Induced Hot Carrier Science and Technology. *Nat. Nanotechnol.* **2015**, *10*, 25-34.

- 10. Zheng, Z.; Majima, T., Nanoplasmonic Photoluminescence Spectroscopy at Single-Particle Level: Sensing for Ethanol Oxidation. *Angew. Chem., Int. Ed. Engl.* **2016,** *55*, 2879-2883.
- 11. Zheng, B. Y.; Zhao, H.; Manjavacas, A.; McClain, M.; Nordlander, P.; Halas, N. J., Distinguishing between Plasmon-Induced and Photoexcited Carriers in a Device Geometry. *Nat. Commun.* **2015**, *6*, 7797.
- 12. Mubeen, S.; Lee, J.; Singh, N.; Krämer, S.; Stucky, G. D.; Moskovits, M., An Autonomous Photosynthetic Device in Which All Charge Carriers Derive from Surface Plasmons. *Nat. Nanotechnol.* **2013**, *8*, 247-251.
- 13. Christopher, P.; Xin, H.; Marimuthu, A.; Linic, S., Singular Characteristics and Unique Chemical Bond Activation Mechanisms of Photocatalytic Reactions on Plasmonic Nanostructures.

  Nat. Mater. 2012, 11, 1044–1050.
- 14. Mukherjee, S.; Zhou, L.; Goodman, A. M.; Large, N.; Ayala-Orozco, C.; Zhang, Y.; Nordlander, P.; Halas, N. J., Hot-Electron-Induced Dissociation of H2 on Gold Nanoparticles Supported on Sio2. *J. Am. Chem. Soc.* **2014**, *136*, 64-67.
- 15. Jin, R.; Charles Cao, Y.; Hao, E.; Métraux, G. S.; Schatz, G. C.; Mirkin, C. A., Controlling Anisotropic Nanoparticle Growth through Plasmon Excitation. *Nature* **2003**, *425*, 487-490.
- 16. Wu, X.; Thrall, E. S.; Liu, H.; Steigerwald, M.; Brus, L., Plasmon Induced Photovoltage and Charge Separation in Citrate-Stabilized Gold Nanoparticles. *J. Phys. Chem. C* **2010**, *114*, 12896-12899.
- 17. Thrall, E. S.; Preska Steinberg, A.; Wu, X.; Brus, L. E., The Role of Photon Energy and Semiconductor Substrate in the Plasmon-Mediated Photooxidation of Citrate by Silver Nanoparticles. *J. Phys. Chem. C* **2013**, *117*, 26238-26247.
- 18. Clavero, C., Plasmon-Induced Hot-Electron Generation at Nanoparticle/Metal-Oxide

- Interfaces for Photovoltaic and Photocatalytic Devices. Nat. Photonics 2014, 8, 95-103.
- 19. Tagliabue, G.; Jermyn, A. S.; Sundararaman, R.; Welch, A. J.; DuChene, J. S.; Pala, R.; Davoyan, A. R.; Narang, P.; Atwater, H. A., Quantifying the Role of Surface Plasmon Excitation and Hot Carrier Transport in Plasmonic Devices. *Nat. Commun.* **2018**, *9*, 3394.
- 20. Sundararaman, R.; Narang, P.; Jermyn, A. S.; Goddard, W. A.; Atwater, H. A., Theoretical Predictions for Hot-Carrier Generation from Surface Plasmon Decay. *Nat. Commun.* **2014**, *5*, 5788.
- 21. Sheldon, M. T.; van de Groep, J.; Brown, A. M.; Polman, A.; Atwater, H. A., Plasmoelectric Potentials in Metal Nanostructures. *Science* **2014**, *346*, 828-831.
- 22. Manjavacas, A.; Liu, J. G.; Kulkarni, V.; Nordlander, P., Plasmon-Induced Hot Carriers in Metallic Nanoparticles. *ACS Nano* **2014**, *8*, 7630-7638.
- 23. Narang, P.; Sundararaman, R.; Jermyn, A. S.; Goddard, W. A.; Atwater, H. A., Cubic Nonlinearity Driven up-Conversion in High-Field Plasmonic Hot Carrier Systems. *J. Phys. Chem. C* **2016**, *120*, 21056-21062.
- 24. Brown, A. M.; Sundararaman, R.; Narang, P.; Goddard, W. A.; Atwater, H. A., Nonradiative Plasmon Decay and Hot Carrier Dynamics: Effects of Phonons, Surfaces, and Geometry. *ACS Nano* **2016**, *10*, 957-966.
- 25. Román Castellanos, L.; Hess, O.; Lischner, J., Single Plasmon Hot Carrier Generation in Metallic Nanoparticles. *Commun. Phys.* **2019**, *2*, 47.
- 26. Khurgin, J.; Tsai, W.-Y.; Tsai, D. P.; Sun, G., Landau Damping and Limit to Field Confinement and Enhancement in Plasmonic Dimers. *ACS Photonics* **2017**, *4*, 2871-2880.
- 27. Heilpern, T.; Manjare, M.; Govorov, A. O.; Wiederrecht, G. P.; Gray, S. K.; Harutyunyan, H., Determination of Hot Carrier Energy Distributions from Inversion of Ultrafast Pump-Probe

- Reflectivity Measurements. Nat. Commun. 2018, 9, 1853.
- 28. Beversluis, M. R.; Bouhelier, A.; Novotny, L., Continuum Generation from Single Gold Nanostructures through near-Field Mediated Intraband Transitions. *Phys. Rev. B: Condens. Matter Mater. Phys* **2003**, *68*, 115433.
- 29. Cai, Y.-Y.; Liu, J. G.; Tauzin, L. J.; Huang, D.; Sung, E.; Zhang, H.; Joplin, A.; Chang, W.-S.; Nordlander, P.; Link, S., Photoluminescence of Gold Nanorods: Purcell Effect Enhanced Emission from Hot Carriers. *ACS Nano* **2018**, *12*, 976-985.
- 30. Lin, K.-Q.; Yi, J.; Hu, S.; Sun, J. J.; Zheng, J. T.; Wang, X.; Ren, B., Intraband Hot-Electron Photoluminescence from Single Silver Nanorods. *ACS Photonics* **2016**, *3*, 1248-1255.
- 31. Tauzin, L. J.; Cai, Y.-Y.; Smith, K. W.; Hosseini Jebeli, S. A.; Bhattacharjee, U.; Chang, W.-S.; Link, S., Exploring the Relationship between Plasmon Damping and Luminescence in Lithographically Prepared Gold Nanorods. *ACS Photonics* **2018**, *5*, 3541-3549.
- 32. Liu, J. G.; Zhang, H.; Link, S.; Nordlander, P., Relaxation of Plasmon-Induced Hot Carriers. *ACS Photonics* **2018**, *5*, 2584-2595.
- 33. Mooradian, A., Photoluminescence of Metals. *Appl. Phys. Lett.* **1969**, *22*, 185-187.
- 34. Boyd, G. T.; Yu, Z. H.; Shen, Y. R., Photoinduced Luminescence from the Noble Metals and Its Enhancement on Roughened Surfaces. *Phys. Rev. B: Condens. Matter Mater. Phys* **1986**, 33, 7923-7936.
- 35. Cai, Y.-Y.; Sung, E.; Zhang, R.; Tauzin, L. J.; Liu, J. G.; Ostovar, B.; Zhang, Y.; Chang, W.-S.; Nordlander, P.; Link, S., Anti-Stokes Emission from Hot Carriers in Gold Nanorods. *Nano Lett.* **2019**, *19*, 1067-1073.
- 36. Hu, H.; Duan, H.; Yang, J. K. W.; Shen, Z. X., Plasmon-Modulated Photoluminescence of Individual Gold Nanostructures. *ACS Nano* **2012**, *6*, 10147-10155.

- 37. Mertens, J.; Kleemann, M.-E.; Chikkaraddy, R.; Narang, P.; Baumberg, J. J., How Light Is Emitted by Plasmonic Metals. *Nano Lett.* **2017**, *17*, 2568-2574.
- 38. Hugall, J. T.; Baumberg, J. J., Demonstrating Photoluminescence from Au Is Electronic Inelastic Light Scattering of a Plasmonic Metal: The Origin of Sers Backgrounds. *Nano Lett.* **2015**, *15*, 2600-2604.
- 39. Sönnichsen, C.; Franzl, T.; Wilk, T.; von Plessen, G.; Feldmann, J.; Wilson, O.; Mulvaney, P., Drastic Reduction of Plasmon Damping in Gold Nanorods. *Appl. Phys. Lett.* **2002**, *88*, 077402.
- 40. van de Hulst, H. C., *Light Scattering by Small Particles*. Dover: New York, **1981**.
- 41. Hartland, G. V., Optical Studies of Dynamics in Noble Metal Nanostructures. *Chem. Rev.* **2011**, *111*, 3858-3887.
- 42. Lin, K.-Q.; Yi, J.; Hu, S.; Liu, B.-J.; Liu, J.-Y.; Wang, X.; Ren, B., Size Effect on Sers of Gold Nanorods Demonstrated Via Single Nanoparticle Spectroscopy. *J. Phys. Chem. C* **2016**, *120*, 20806-20813.
- 43. Foerster, B.; Joplin, A.; Kaefer, K.; Celiksoy, S.; Link, S.; Sönnichsen, C., Chemical Interface Damping Depends on Electrons Reaching the Surface. *ACS Nano* **2017**, *11*, 2886-2893.
- 44. Yorulmaz, M.; Khatua, S.; Zijlstra, P.; Gaiduk, A.; Orrit, M., Luminescence Quantum Yield of Single Gold Nanorods. *Nano Lett.* **2012**, *12*, 4385-4391.
- 45. Andersen, S. K. H.; Pors, A.; Bozhevolnyi, S. I., Gold Photoluminescence Wavelength and Polarization Engineering. *ACS Photonics* **2015**, *2*, 432-438.
- 46. Novo, C.; Gomez, D.; Perez-Juste, J.; Zhang, Z.; Petrova, H.; Reismann, M.; Mulvaney, P.; Hartland, G. V., Contributions from Radiation Damping and Surface Scattering to the Linewidth of the Longitudinal Plasmon Band of Gold Nanorods: A Single Particle Study. *Phys. Chem. Chem. Phys.* **2006**, *8*, 3540-3546.

- 47. Sivun, D.; Vidal, C.; Munkhbat, B.; Arnold, N.; Klar, T. A.; Hrelescu, C., Anticorrelation of Photoluminescence from Gold Nanoparticle Dimers with Hot-Spot Intensity. *Nano Lett.* **2016**, *16*, 7203–7209.
- 48. Cai, Y.-Y.; Collins, S. S. E.; Gallagher, M. J.; Bhattacharjee, U.; Zhang, R.; Chow, T. H.; Ahmadivand, A.; Ostovar, B.; Al-Zubeidi, A.; Wang, J.; Nordlander, P.; Landes, C. F.; Link, S., Single-Particle Emission Spectroscopy Resolves D-Hole Relaxation in Copper Nanocubes. *ACS Energy Lett.* **2019**, *4*, 2458-2465.
- 49. Zhang, W.; Cheng, Y.; Zhao, J.; Wen, T.; Hu, A.; Gong, Q.; Lu, G., Photoluminescence Quantum Yield from Gold Nanorods: Dependence on Excitation Polarization. *J. Phys. Chem. C* **2019**, *123*, 9358-9363.
- 50. Tcherniak, A.; Dominguez-Medina, S.; Chang, W.-S.; Swanglap, P.; Slaughter, L. S.; Landes, C. F.; Link, S., One-Photon Plasmon Luminescence and Its Application to Correlation Spectroscopy as a Probe for Rotational and Translational Dynamics of Gold Nanorods. *J. Phys. Chem. C* **2011**, *115*, 15938-15949.
- 51. Joplin, A.; Chang, W.-S.; Link, S., Imaging and Spectroscopy of Single Metal Nanostructure Absorption. *Langmuir* **2018**, *34*, 3775-3786.
- 52. Bohren, C. F.; Huffman, D. R., Absorption and Scattering of Light by Small Particles. Wiley: New York: 1983.
- 53. Kreibig, U.; Vollmer, M., Optical Properties of Metal Clusters. Springer: Berlin, 1995.
- 54. Koenderink, A. F., On the Use of Purcell Factors for Plasmon Antennas. *Opt. Lett.* **2010,** 35, 4208-4210.
- 55. Fröhlich, T.; Schönenberger, C.; Calame, M., Additional Peak Appearing in the One-Photon Luminescence of Single Gold Nanorods. *Opt. Lett.* **2016**, *41*, 1325-1328.

- 56. Gaiduk, A.; Yorulmaz, M.; Orrit, M., Correlated Absorption and Photoluminescence of Single Gold Nanoparticles. *ChemPhysChem* **2011**, *12*, 1536-1541.
- 57. Qu, S.; Li, H.; Peng, T.; Gao, Y.; Qiu, J.; Zhu, C., Optical Nonlinearities from Transverse Plasmon Resonance in Gold Nano-Rods. *Mater. Lett.* **2004**, *58*, 1427-1430.
- 58. Hohenester, U.; Trügler, A., Mnpbem a Matlab Toolbox for the Simulation of Plasmonic Nanoparticles. *Comput. Phys. Commun.* **2012**, *183*, 370-381.
- 59. Shang, L.; Dong, S., Design of Fluorescent Assays for Cyanide and Hydrogen Peroxide Based on the Inner Filter Effect of Metal Nanoparticles. *Anal. Chem.* **2009**, *81*, 1465-1470.
- 60. Novotny, L.; Hecht, B., *Principles of Nano-Optics* Cambridge University Press: Cambridge, **2006**.
- 61. Bosman, M.; Zhang, L.; Duan, H.; Tan, S. F.; Nijhuis, C. A.; Qiu, C. W.; Yang, J. K. W., Encapsulated Annealing: Enhancing the Plasmon Quality Factor in Lithographically–Defined Nanostructures. *Sci. Rep.* **2014**, *4*, 5537.
- 62. Sauvan, C.; Hugonin, J. P.; Maksymov, I. S.; Lalanne, P., Theory of the Spontaneous Optical Emission of Nanosize Photonic and Plasmon Resonators. *Appl. Phys. Lett.* **2013**, *110*, 237401.
- 63. Ruppin, R., Electromagnetic Energy Density in a Dispersive and Absorptive Material. *Phys. Lett. A* **2002**, *299*, 309-312.
- 64. Johnson, P. B.; Christy, R. W., Optical Constants of the Noble Metals. *Phys. Rev. B* **1972**, 6, 4370-4379.
- 65. Olmon, R. L.; Slovick, B.; Johnson, T. W.; Shelton, D.; Oh, S.-H.; Boreman, G. D.; Raschke, M. B., Optical Dielectric Function of Gold. *Phys. Rev. B: Condens. Matter Mater. Phys.* **2012**, *86*, 235147.

- 66. Shen, H.; Lu, G.; Zhang, T.; Liu, J.; Gu, Y.; Perriat, P.; Martini, M.; Tillement, O.; Gong, Q., Shape Effect on a Single-Nanoparticle-Based Plasmonic Nanosensor. *Nanotechnology* **2013**, *24*, 285502.
- 67. Kumar, M.; Dey, J.; Verma, M. S.; Chandra, M., Nanoscale Plasmon–Exciton Interaction: The Role of Radiation Damping and Mode-Volume in Determining Coupling Strength. *Nanoscale* **2020,** *12*, 11612-11618.
- 68. Zhang, H.; Govorov, A. O., Optical Generation of Hot Plasmonic Carriers in Metal Nanocrystals: The Effects of Shape and Field Enhancement. *J. Phys. Chem. C* **2014**, *118*, 7606-7614.
- 69. Ye, X.; Zheng, C.; Chen, J.; Gao, Y.; Murray, C. B., Using Binary Surfactant Mixtures to Simultaneously Improve the Dimensional Tunability and Monodispersity in the Seeded Growth of Gold Nanorods. *Nano Lett.* **2013**, *13*, 765-771.
- 70. Ming, T.; Feng, W.; Tang, Q.; Wang, F.; Sun, L.; Wang, J.; Yan, C., Growth of Tetrahexahedral Gold Nanocrystals with High-Index Facets. *J. Am. Chem. Soc.* **2009**, *131*, 16350-16351.
- 71. Huang, D.; Byers, C. P.; Wang, L.-Y.; Hoggard, A.; Hoener, B.; Dominguez-Medina, S.; Chen, S.; Chang, W.-S.; Landes, C. F.; Link, S., Photoluminescence of a Plasmonic Molecule. *ACS Nano* **2015**, *9*, 7072-7079.
- 72. Martinsson, E.; Shahjamali, M. M.; Large, N.; Zaraee, N.; Zhou, Y.; Schatz, G. C.; Mirkin, C. A.; Aili, D., Influence of Surfactant Bilayers on the Refractive Index Sensitivity and Catalytic Properties of Anisotropic Gold Nanoparticles. *Small* **2016**, *12*, 330-342.